Solar Phys (2010) 265: 19–30
DOI 10.1007/s11207-010-9557-9

Three-Dimensional Electron Density from Tomographic Analysis of LASCO-C2 Images of the K-Corona Total Brightness

Richard A. Frazin · Philippe Lamy · Antoine Llebaria · Alberto M. Vásquez

Received: 27 November 2009 / Accepted: 7 April 2010 / Published online: 8 May 2010

Abstract We present the first quantitative three-dimensional (3D) tomographic reconstructions of electron density from coronagraph measurements of the K-corona's total brightness (B) made by LASCO-C2 on SOHO. This is possible because new calibrations of the LASCO-C2 images in both polarized brightness (pB) and B have now been made for the entire mission. The B and pB reconstructions are compared, and the differences are explained in terms of line of sight weighting functions in Thomson scattering. We conclude that the LASCO-C2 B archive, which is vastly larger than the pB archive, will be a very valuable resource for determining the 3D electron density throughout the SOHO mission which started taking data in 1996.

Keywords Solar corona · Tomography · Electron density · Thomson scattering

Remote Sensing of the Inner Heliosphere
Guest Editors: M.M. Bisi and A.R. Breen

R.A. Frazin (✉)
Dept. of Atmospheric, Oceanic and Space Sciences, University of Michigan,
Ann Arbor, MI 48109, USA
e-mail: rfrazin@umich.edu

P. Lamy · A. Llebaria
Laboratoire d'Astrophysique de Marseille, Université de Provence – CNRS, 38 rue Frédéric Joliot-Curie, 13388 Marseille cedex 13, France

P. Lamy
e-mail: philippe.lamy@oamp.fr

A. Llebaria
e-mail: antoine.llebaria@oamp.fr

A.M. Vásquez
Instituto de Astronomía y Física del Espacio, CONICET – University of Buenos Aires, CC 67 Suc 28, Ciudad de Buenos Aires, Argentina
e-mail: albert@iafe.uba.ar

1. Introduction

The Large Angle and Spectrometric Coronagraph Experiment (LASCO) on the SOHO spacecraft has been operating nearly continuously since late 1995 (Brueckner *et al.*, 1995), and the two coronagraphs C2 and C3 provide an invaluable data set spanning more than a full solar cycle. The Laboratoire d'Astrophysique de Marseille [formerly Laboratoire d'Astronomie Spatiale (LAS)] has recently determined the calibration for both the total coronal brightness (B) and the polarized brightness (pB)[1] of the K-corona for the entire LASCO-C2 data set, making C2 the best characterized space-based, white-light coronagraph in history, with the possible exception of the single-pixel Ultraviolet Coronagraph Spectrometer (UVCS) White Light Channel (Kohl *et al.*, 1995). This effort required modeling the contributions to the signal made by the F-corona, stray light, and a number of other instrumental effects (e.g., spatial variation in the transmission of the polaroid sheets, polarization by the folding mirrors). The C2 instrument has taken vastly more unpolarized images than pB sequences (each of which is a series of three images with the polarizers oriented at 60° from each other, with an additional image without the polarization filters), with only one pB sequence per day made throughout most of the mission. Thus, this calibration makes possible quantitative photometric analysis of a comprehensive data set containing many images per day going back to the year 1996. As discussed in Frazin *et al.* (2007), the standard pB cadence of one per day limits the spatial resolution that can be achieved with tomographic reconstruction. Thus, the addition of these new data has the potential to increase significantly the detail available from tomographic methods.

While compromised by the Sun's temporal variations, tomography is the only model-independent way of determining the electron density (N_e) of the global corona. [For general discussions of tomographic 3D reconstruction of the solar corona see Frazin and Janzen (2002) and Frazin, Vásquez, and Kamalabadi (2009).] Knowledge of N_e is critical for constraining solar wind models (Vásquez *et al.*, 2008), determination of the background solar wind structure for CME propagation (Manchester *et al.*, 2005), and spectroscopic diagnostics (Frazin, Cranmer, and Kohl, 2003), to name a few. The problem of determining N_e from B images was first considered by Hayes, Vourlidas and Howard (2001). They applied the spherically symmetric inversion method invented by van de Hulst (1950) to C2 images, but not with the calibration used here, and instead used a combined model of the stray light and F-corona. Quémerais and Lamy (2002) used a more advanced instrument calibration (the predecessor to the one used here) and an advanced F-corona removal scheme (again, the predecessor to the one used here) to compute both cylindrically and spherically symmetric inversions of both pB and B C2 images. They found the resulting electron densities from the two types of images to be quite consistent with each other, validating the calibration and F-corona model. Morgan, Habbal, and Lugaz (2009) and Morgan and Habbal (2010) applied the backprojection technique to C2 B images to obtain qualitative 3D reconstructions, in the latter case over a solar cycle.

In a theoretical study, Frazin and Kamalabadi (2005) considered the impact of the information contained in B images on tomographic reconstruction of the corona's 3D density distribution. The source of this extra information is the difference between the line of sight (LOS) weighting of the electron density in the B and pB images. The conclusion of this work was that if the K-corona B images have a signal-to-noise ratio comparable to, or better than, that of the pB images (which requires an accurate F-corona model), the B images

[1] For the sake of convenience and convention, the nomenclature "pB" represents the product $p_K B_K$ seen in Equation (2) below.

have about as much information as the pB images and the combination of B and pB images can lead to improved estimates of the 3D N_e. Indeed, the information provided by this difference in the LOS weightings was exploited by Moran and Davila (2004) to estimate the distance from the plane of the sky of a CME from a single pB sequence (which allows the computation of both B and pB images).

2. Calibration and Separation of the K and F Coronae

The absolute calibration of the total intensity (B_T) images relies on the photometry of the stars present in the C2 field of view (FOV), and was implemented by Llebaria, Lamy, and Danjard (2006). The absolute calibration of the pB images is obtained by relating the B_T image calculated from the triplet of polarized images to the B_T unpolarized image which brackets the triplet. The temporal variation of the ratio between the resulting B_T images (probably resulting from the differential aging between the polarizer channels and the neutral one) is taken into account.

The observed total intensity (*i.e.*, the first component of the Stokes vector) B_T seen by the LASCO-C2 coronagraph amounts to

$$B_T = B_K + B_F + B_S, \tag{1}$$

where B_K is the K-corona total intensity, and B_F is the F-corona total intensity. The stray light B_S mostly results from light diffracted by the various occulters, apertures and stops, and it is therefore axially symmetric (except for a narrow sector corresponding to the pylons supporting the occulters) and unpolarized (the polarized fraction of the stray light $p_S = 0$) to first order. The polarized part of the total intensity $p_T B_T$ (*i.e.*, the second component of the Stokes vector in the appropriate coordinate system) therefore involves only the K and F components of the corona:

$$p_T B_T = p_K B_K + p_F B_F, \tag{2}$$

where p_K is the K-corona polarized fraction. Equation (2) shows that, in its most general form, the problem of separating B_K and B_F using Equations (1) and (2) is intractable. We therefore make use of the classical assumption that the polarized fraction of the F-corona intensity $p_F = 0$, which is valid in the FOV of C2, so that the observed polarized intensity is simply

$$p_T B_T = p_K B_K. \tag{3}$$

The F-corona introduces some polarization at larger elongations. The elongation at which the F-corona contribution to the polarization becomes significant has been claimed to be as low as four solar radii (R_s) (Hayes, Vourlidas, and Howard, 2001), although Blackwell and Petford (1966a, 1966b) claim it is much higher. The fractional polarization of the F-corona is discussed in Koutchmy and Lamy (1985) and values are given. At this point, we have to assume a model of p_K and this is justified by the robust "asymptotic" behavior of $p_K(r)$ beyond 2.2 R_s, which is almost independent of the coronal electron density profiles. Therefore our first determination of B_K is given by:

$$B_K = p_T B_T / p_K. \tag{4}$$

This separation is not perfect and significant traces of the K-corona are present in the other component which, in the ideal case, should only be a superposition of the F-corona

and stray light. This situation mostly results from the inherent limitations of using three (imperfect) polarizers. In order to construct an F-corona model free of K-corona traces, we proceed following the method described by Llebaria, Loirat, and Lamy (2010). We assume an F-corona model whose spatio-temporal variation can be described by a small number of parameters. Spatially, it is specified by an exponential functions of few parameters, and temporally, the variation, mostly due to orbital geometric effects on the line of sight, is specified by at most nine Fourier components. Using related methods, Morgan and Habbal (2007) argue that the F-corona exhibits a high degree of temporal stability. Like the F-corona, the stray light varies during the year, but at a different level and with a different profile. This fact, as well as the assumed central symmetry of the mean F-corona is exploited to separate the F-corona from the stray light. Finally, with the variable stray light and with the restored variable F-corona accurately determined for each day, we obtain a second much more accurate determination of the K-corona by subtraction of the F-corona and stray light from the high-cadence series of LASCO-C2 images.

3. LOS Weighting

In the Thomson scattering process, the light scattered by the free electrons (K-corona) is polarized with the polarization vector tangent to the limb in polarized images. Schuster (1897) was the first to calculate the polarized scattering from the K-corona, taking into account integration over the solid angle subtended by the Sun (including limb-darkening), and his work was later corrected by Minnaert (1930). The scattering discussion by Altschuler (1979) is relatively easy to follow. The resulting formulae of the weighting of the LOS integral are complicated, but, for heights above about 2 R_s, there is little numerical difference between these expressions and much simpler ones that consider the Sun to be a point source. In order to provide physical insight, we provide the point source expressions below.

Consider a point source with luminosity $4\pi L$, and a LOS with a distance of closest approach p (impact parameter), as depicted in Figure 1. The small volume of scattering material under consideration is a distance r from the luminous point source and a distance l from the point of closest approach of the LOS. Thus, the segments with lengths p and l form the legs of a right triangle with hypotenuse $r = \sqrt{p^2 + l^2}$, with l being distance along the LOS. It is convenient to define a scattering angle $\sin\theta \equiv p/r$. The point source emits unpolarized light, so the radiation impinging upon the scattering material is represented by two polarization components, each containing $1/2$ of the energy flux and perpendicular to the hypotenuse of the triangle. The first polarization component is directed out of the triangle's plane (i.e., the plane of Figure 1) and the second is in the plane. The free electrons in the volume re-radiate the same polarizations that excite them with efficiency proportional to the density of free electrons N_e times the Thomson cross section σ_e. The radiation seen by the observer does not have any polarization component parallel to the LOS. One determines the polarization-dependent LOS weighting simply by taking the polarization incident on the scattering volume and removing the component parallel to the LOS. Note that it is the out-of-plane component that is seen as the tangential component by the observer and it is the

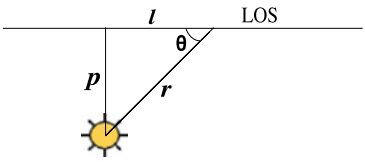

Figure 1 The scattering geometry for Section 3.

in-plane component that is seen as the radial component. The tangential intensity incident on the volume is simply $L/2r^2 = (L/2p^2)(p^2/r^2) = (L/2p^2)\sin^2\theta$, where the $1/2$ factor accounts for the fact that $1/2$ of the incident radiation is polarized out of the plane. This polarization component is also perpendicular to the LOS, so it is scattered into the LOS without any projection effect. Thus, the tangential emissivity is

$$\eta_{\rm t} = \frac{3\sigma_{\rm e}}{8}\frac{L}{2r^2}N_{\rm e} = \frac{3\sigma_{\rm e}}{16}\frac{L}{p^2}\sin^2\theta\, N_{\rm e}. \tag{5}$$

The incident, in-plane component is the same as the incident tangential component, $(L/2p^2)\sin^2\theta$, but this component is itself resolved into two components, one parallel to and the other perpendicular to the LOS. The parallel component does not get scattered into the LOS, so a $\cos^2\theta$ factor must applied, resulting in

$$\eta_{\rm r} = \frac{3\sigma_{\rm e}}{8}\frac{L}{2p^2}\sin^2\theta\cos^2\theta\, N_{\rm e}. \tag{6}$$

Now, the total brightness B is the LOS integral of $\eta_{\rm t} + \eta_{\rm r}$, and the polarized brightness pB is the LOS integral of the difference $\eta_{\rm t} - \eta_{\rm r}$, and we have:

$$B = \frac{3\sigma_{\rm e}}{8}\frac{L}{p^2}\int_{-\infty}^{\infty} {\rm d}l\, N_{\rm e}(l)\left(\sin^2\theta(l) - \frac{1}{2}\sin^4\theta(l)\right), \tag{7}$$

$$pB = \frac{3\sigma_{\rm e}}{16}\frac{L}{p^2}\int_{-\infty}^{\infty} {\rm d}l\, N_{\rm e}(l)\sin^4\theta(l). \tag{8}$$

Thus, the LOS weighting for pB is much more confined to small values of l (*i.e.*, θ near 90°) because $\sin^4\theta$ is much more sharply peaked than $\sin^2\theta$. Figure 2 shows the difference between the weightings for pB and B scattering at 1.5 and 5 $R_{\rm s}$. The figure was calculated using the full expressions, not the point source approximations in Equations (7) and (8), although the differences are negligible for the 5 $R_{\rm s}$ curve.

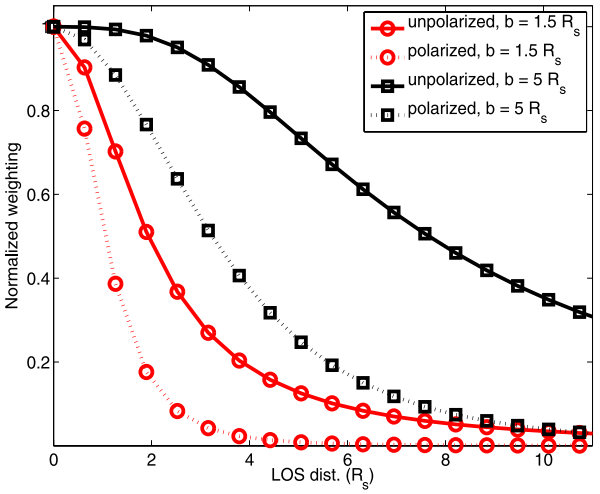

Figure 2 Normalized weighting of the LOS integrals for the polarized and unpolarized K-corona signal at projected radii of $b = 1.5$ and $b = 5.0$ $R_{\rm s}$. The x-axis is the distance along the LOS and y-axis is normalized by the maximum value of the weighting function.

4. The FOV Effect

Tomographic reconstruction of the solar corona in white light is complicated by the occulter, which prevents views from projected radii $r_p < r_o$, where r_p is the projected distance from the Sun center in a coronagraph image and r_o is the occultation radius (effectively $\approx 2.2\ R_s$ for C2). Images with this property are known as *hollow projections* in the tomography literature. Mathematically, it is possible to uniquely reconstruct the density a distance r from the center of the Sun given projection data (*i.e.*, LOS integrals of the object) at $r_p > r$, covering 180° of view angles (Louis and Natterer, 1983). Strictly speaking, in other applications of tomography (e.g., medicine) where the object to be reconstructed is contained within a distance r_s from the center (*i.e.*, the object support), one needs data with projection radii out to r_s to reconstruct it. Restricting the data to $r_p < r_s$ does not provide enough information for unique reconstruction for *any* part of the object. The corona, for the purposes considered here, has infinite extent and therefore any coronagraph with a finite FOV cannot, strictly speaking, provide the required data to uniquely reconstruct any of the corona. In the medical tomography literature, this is known as the interior reconstruction problem, and it has been addressed with a variety of methods (Faridani *et al.*, 2001; Anastasio *et al.*, 2007).

To put these considerations in terms of the specific problem of tomographic reconstruction from LASCO-C2 images, we must consider that the "coronal" plasma extends to a vast distance and fills the solar system. Thus, each pixel of the coronagraph images sees emission from a LOS that contains non-negligible contributions from a path length of tens of solar radii, while the C2 FOV extends only to about 6.1 solar radii. The fact that the density decreases rapidly with distance from the Sun (exponentially at low heights where it is essentially hydrostatic and quadratically at larger heights where the velocity is constant), allows practical reconstruction. The tomographic model has an arbitrary computation domain, and simulation experiments not reported here show that the reconstructions are improved over our previous efforts by extending the computation sphere to $r_c = 8.0\ R_s$. Our previous efforts had the outer radius of the computation sphere set to $r_c = 6.1\ R_s$, the same radius as the C2 FOV (Frazin *et al.*, 2007; Vásquez *et al.*, 2008). The larger radius greatly reduces the build-up of material between 5.5 and 6.1 R_s in the reconstruction, although there is little meaning to the solutions beyond 6.1 R_s.

It is expected that artifacts due to the finite FOV will be more pronounced in reconstructions from B images than those with pB images due to the broader LOS weighting in Equation (7) than in Equation (8). One way to understand this is as follows: obviously, the measured pB and B values come from integrating the LOS over the corona/heliosphere that is vast in extent. Now consider the Sun's corona as it is, except multiplied by 0 in the region $r > r_c$. The pB and B integrals calculated for this case cannot match the measured values due to the truncation. However, the pB values calculated in this case will be closer to the measured pB values, than the so-calculated B values will be to the measured B values. This is because the pB integrals are more heavily weighted toward the 90° scattering point, as can be seen in Figure 2. Thus, we can expect some superior performance from tomographic density determination from pB because finite computation grid allows for a more accurate model of the relationship between the intensity and electron density. A comprehensive study of FOV effects in tomography of the corona is well beyond the scope of this paper and is the subject of a forthcoming study by Frazin and colleagues.

5. Data and Results

In order to create a pB image, C2 takes three exposures of the corona, each through a linear polarizer with a different orientation of the fast axis. For calibration purposes, an unpolarized exposure of same size completes the set. This sequence of three plus one exposures is known as a pB *sequence*. A pB sequence allows calculation of both a pB image and a B image. B images are also measured directly with no polarization elements (after B_F and stray light subtraction), and this type of measurement is much more common for C2. The data used for the reconstructions shown here are taken from a high-cadence set of pB sequences, with about 4 images per day (as opposed to the usual rate of one per day). The data set used consists of 52 pB sequences, roughly evenly spaced in time, starting at about 21:00 UT on 15 March 2009 and ending at about 15:00 UT on 29 March, which falls within Carrington Rotation 2081. Each pB sequence was used to calculate both a pB and B image.

Figures 3 through 5 show slices of the first quantitative tomographic determinations of the coronal N_e from B images. The tomographic grid used is a hollow sphere with grid cells equally spaced in radius, latitude and longitude (Frazin *et al.*, 2007; Vásquez *et al.*, 2008). The minimum radius of the grid is 2.3 R_s, and the maximum is 8.0 R_s, which is greater than the C2 FOV. Extending the volume in this way greatly reduces the density "pile up" at the edge, as described in Section 4. The grid has 60 radial bins (0.095 R_s each), 60 latitude bins and 120 longitude bins. The most recent description of this tomographic inversion scheme and other details about the computation can be found in Frazin, Vásquez, and Kamalabadi (2009).

The top panel of Figure 3 shows N_e derived from tomographic analysis of the B images on a spherical shell with radius 2.5 R_s as a function of latitude and longitude. The zero density regions near the streamer belt are artifacts due to the Sun's dynamics, and they were

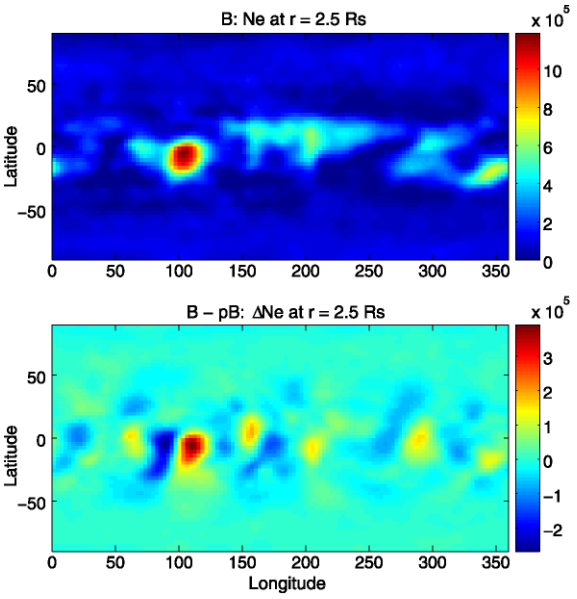

Figure 3 Upper panel: N_e (units cm^{-3}) at 2.5 R_s as a function of latitude and longitude from tomography based on B images. Lower panel: At the same height, ΔN_e, *i.e.*, the N_e value derived from tomographic inversion of B images minus that from pB images. The data used for the tomographic reconstruction are for Carrington Rotation 2081.

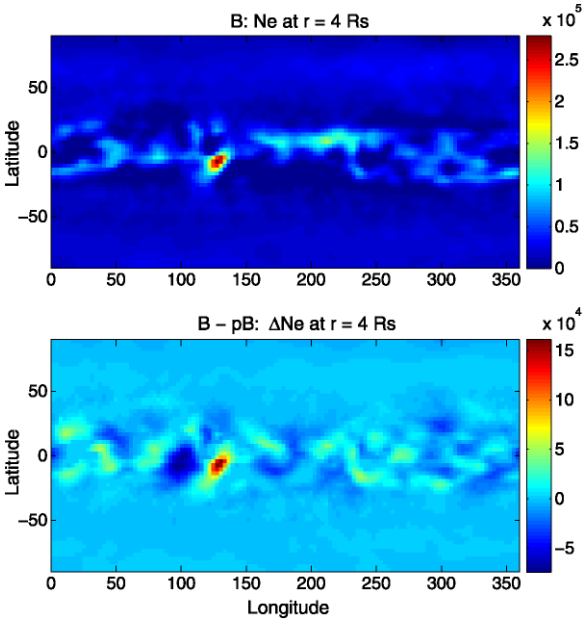

Figure 4 Similar to Figure 3, except at 4 R_s.

first identified in Frazin and Janzen (2002).[2] The bottom panel also shows a spherical shell with radius 2.5 R_s as a function of latitude and longitude, but of the difference of the two tomographic reconstructions: $N_e(B) - N_e(pB)$. In this notation, $N_e(B)$ is the density derived from the B images (as in the top panel), and $N_e(pB)$ is the density derived from pB images. We have chosen to display the difference because the $N_e(B)$ and $N_e(pB)$ reconstructions have very similar visual appearances. The color scale of this difference image is also in units of cm^{-3}. Figures 4 and 5 are similar to Figure 3, except at heights of 4.0 and 5.5 R_s, respectively.

For more quantitative comparisons, we define the solid angle average of the density from pB images at a given radius r as:

$$M_{pB}(r) \equiv \frac{1}{4\pi} \int_{-\pi/2}^{\pi/2} \mathrm{d}\theta \, \cos\theta \int_0^{2\pi} \mathrm{d}\phi \, N_e(pB)(r, \theta, \phi), \tag{9}$$

where θ and ϕ are the Carrington latitude and longitude, respectively, and $N_e(pB)(r, \theta, \phi)$ is the reconstruction from pB data. The quantity $M_B(r)$ has a similar definition, except $N_e(B)(r, \theta, \phi)$ is replaced with $N_e(B)(r, \theta, \phi)$. Both $M_B(r)$ and $M_{pB}(r)$ are proportional to the mass of the plasma in a finite-width spherical shell of radius r. Equation (9) cannot be used directly on the tomographic quantities for two reasons. The first, and most obvious, is that the tomographic quantities are defined on grid, so the integrals must be replaced by appropriate sums. The second issue is that the reconstructions have zero density artifacts, and these regions should not be included in any type of analysis. To calculate the functions $M_B(r)$ and $M_{pB}(r)$, we excluded voxels where $N_e(B) < 100$ cm^{-3} or $N_e(pB) < 100$ cm^{-3} (the normalization of the integral was appropriately adjusted). Such voxels, in which either

[2]Such defects in the reconstructions, called *zero density artifacts*, are due to the fact that the tomographic process does not take coronal dynamics into account (Frazin and Janzen, 2002; Butala *et al.*, 2010).

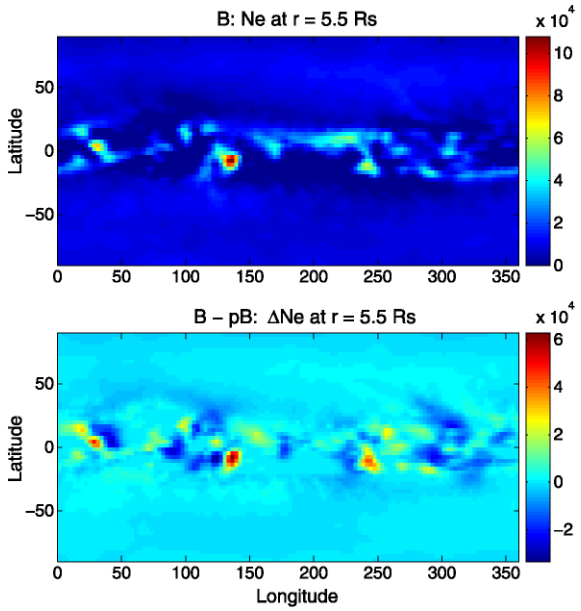

Figure 5 Similar to Figure 3, except at 5.5 R_S.

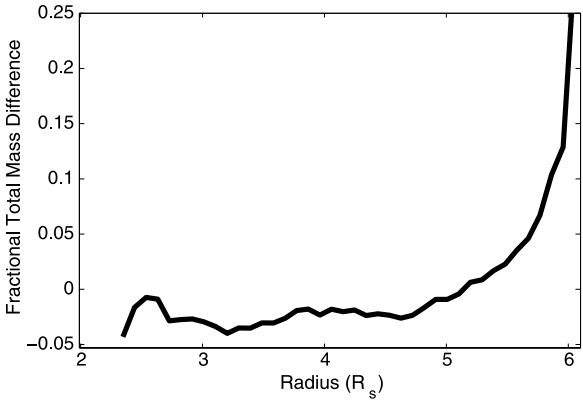

Figure 6 The mean fractional difference in the mass of spherical shells of the B and pB reconstructions as a function of distance from Sun center [see Equation (9)]. This shows that below about 5.5 R_S the spherical shells from the pB reconstructions have slightly more mass than those of B. Above that height edge effects make the shells of the B reconstruction more massive.

reconstructed density is below 100 cm^{-3}, represent about 7.5% of the population (considering only the portion of the tomographic grid between 2.3 and 6.1 R_s). Figure 6 compares the fractional differences of the total masses in a given spherical shell of the B and pB reconstructions. Clearly, below about 5.5$N_e(pB)$ is about 1 – 5% greater, but beyond, the average $N_e(B)$ goes up to about 25% greater than the average $N_e(pB)$. This density excess at the edge of the FOV, although mitigated by extending the grid to 8.0 R_s, is most likely due to the effect of FOV truncation and the difference in the LOS weighting between pB and B scattering, as described in Section 4.

Another measure of agreement between the two reconstructions at given voxel defined by coordinates (r, θ, ϕ), called the *absolute fractional difference*, is:

$$\delta(r,\theta,\phi) \equiv 2\frac{\|N_e(B)(r,\theta,\phi) - N_e(pB)(r,\theta,\phi)\|}{N_e(pB)(r,\theta,\phi) + N_e(B)(r,\theta,\phi)}. \tag{10}$$

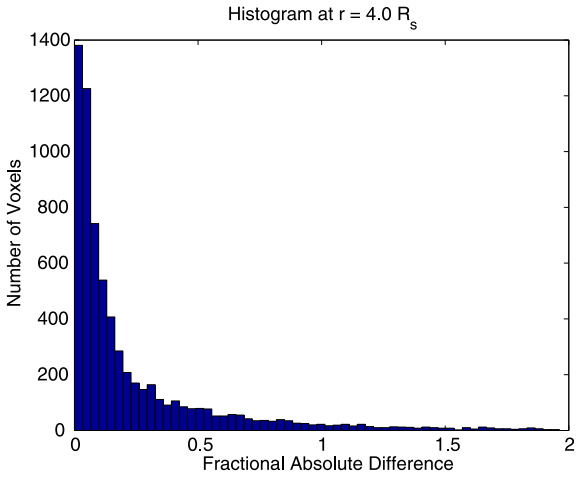

Figure 7 A histogram of the absolute fractional differences in the pB and B reconstructions at 4 R_S. The y-axis is the number of voxels (on the shell of the of the spherical grid containing the sphere of radius 4 R_S) and the x-axis is the absolute fractional difference δ in Equation (10). This distribution is roughly exponential in character. The histograms for the other radial bins all have this shape, but the width varies (see Figure 8).

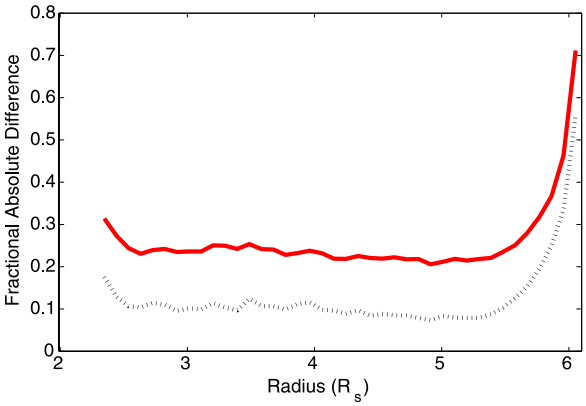

Figure 8 The mean (solid red curve) and median (dashed black curve) value of the distributions of the absolute fractional deviation δ between B and pB reconstructions [see Equation (10)], as function of radius. These curves are derived from histograms made at each radius, an example of which is shown in Figure 7.

For Figures 7 and 8, we excluded voxels where $N_e(B) < 100$ cm^{-3} or $N_e(pB) < 100$ cm^{-3}, as above. Figure 7 shows a histogram of the δ values for the voxels centered at 4.0 R_s. This distribution is roughly exponential in appearance, as are the corresponding distributions for all of the other radial bins below 6.1 R_s (above that height, the reconstructions have little meaning, as discussed in Section 4). For each radial bin in the tomographic grid, we made a histogram similar to that shown in Figure 7, and plotted the mean (median) of the distributions as the solid red (black dashed) curve in Figure 8. For most heights, median of the δ distribution is about 0.1, meaning that 50% of the voxels of the two reconstructions agree to 10% or better, and the mean is about 25%, indicating that some voxels have larger disagreements. These values can be understood by examining Figure 7. Above about 5.5 R_s the mean and median increase, and this is due to the "pile-up" effect described in Section 4. The increase near 2.3 R_s in Figure 8 is most likely caused by the difficulty in determining the stray light level in the B images due to the diffraction rings.

6. Conclusions

Due to the extensive effort made by the Laboratoire d'Astrophysique de Marseille to characterize LASCO-C2 and model the F-corona, we were able to perform the first quantitative tomographic reconstructions of N_e based on K-corona total intensity (B) images. This capability is important because the B images outnumber the pB images by more than an order of magnitude and have fewer gaps. We compared the 3D tomographic N_e reconstructions based on both B and pB data. Since B has a broader scattering function than pB does, we expect the FOV effects to be more important in reconstructions from B than pB. The effects of FOV truncation and the angular width of the scattering functions on tomography is the subject of a forthcoming study. As Figure 6 shows, the typical difference between the two determinations of the mass in a given spherical shell is less than 5%, except above about 5.5 R_s. Above that height, a complicated interaction between the effects of coronagraph FOV truncation and the difference between the angular scattering functions of B and pB has a more obvious effect. While the shell masses are in good agreement, and Figure 8 shows that most of the voxels' absolute fractional differences [δ in Equation (10)] agree to within 10%, there is a significant population of voxels with much larger disagreement making the mean value of δ about 25%. The δ values are larger above 5.5 R_s due to edge effects, and they are also larger below 2.5 R_s due to some difficulty in determining the stray light contributions to the B images where diffraction rings are prominent.

It is our intention to utilize this new data set to produce high quality, quantitative, 3D reconstructions of N_e for the full LASCO mission. In order to lessen the impact of coronal dynamics on the reconstructions, we intend to apply a time-dependent formulation of tomographic reconstruction (Frazin *et al.*, 2005; Butala *et al.*, 2009; Butala *et al.*, 2010).

Acknowledgements This research was supported by NASA Heliophysics Guest Investigator award NNX08AJ09G to the University of Michigan. The LASCO-C2 project at the Laboratoire d'Astrophysique de Marseille (formerly Laboratoire d'Astronomie Spatiale) is funded by the Centre National d'Etudes Spatiales (CNES). LASCO was built by a consortium of the Naval Research Laboratory, USA, the Laboratoire d'Astronomie Spatiale in Marseille, France, the Max Planck Institute für Aeronomie in Lindau, Germany, and the School of Physics and Astronomy, University of Birmingham, UK. SoHO is a project of joint collaboration by ESA and NASA.

References

Altschuler, M.D.: 1979, In: Herman, G.T. (ed.) *Image Reconstruction from Projections: Implementation and Applicaitons*, Springer, Berlin.

Anastasio, M.A., Zou, Y., Sidky, E.Y., Pan, X.: 2007, *J. Opt. Soc. Am. A* **24**, 1569.

Blackwell, D.E., Petford, A.D.: 1966a, *Mon. Not. R. Astron. Soc.* **131**, 383.

Blackwell, D.E., Petford, A.D.: 1966b, *Mon. Not. R. Astron. Soc.* **131**, 399.

Brueckner, G.E., Howard, R.A., Koomen, M.J., Korendyke, C.M., Michels, D.J., Moses, J.D., Socker, D.G., Dere, K.P., Lamy, P.L., Llebaria, A., *et al.*: 1995, *Solar Phys.* **162**, 357.

Butala, M.D., Frazin, R.A., Chen, Y., Kamalabadi, F.: 2009, *IEEE Trans. Image Process.* **18**, 1573.

Butala, M.D., Hewett, R.J., Frazin, R.A., Kamalabadi, F.: 2010, *Solar Phys.* **262**, 495. doi:10.1007/s11207-010-9536-1.

Faridani, A., Buglione, K., Huabsomboon, P., Iancu, O., McGrath, J.: 2001, In: Tinto, E.T., Ehrenpreis, L., Faridani, A., Gonzalez, F., Grinberg, E. (eds.) *Radon Transforms and Tomography*, *2000 AMS-IMS-SIAM Joint Summer Research Conference on Radon Transforms and Tomography, Mount Holyoke College*, *South Hadley, Massachusetts*, *June 18–22, 2000*, American Mathematical Society, New York, 29.

Frazin, R.A., Janzen, P.: 2002, *Astrophys. J.* **570**, 408.

Frazin, R.A., Kamalabadi, F.: 2005, *Astrophys. J.* **628**, 1061.

Frazin, R.A., Cranmer, S.R., Kohl, J.L.: 2003, *Astrophys. J.* **597**, 1145.

Frazin, R.A., Vásquez, A.M., Kamalabadi, F.: 2009, *Astrophys. J.* **701**, 547.

Frazin, R.A., Butala, M.D., Kemball, A., Kamalabadi, F.: 2005, *Astrophys. J. Lett.* **635**, L197.
Frazin, R.A., Vásquez, A.M., Kamalabadi, F., Park, H.: 2007, *Astrophys. J. Lett.* **671**, L201.
Hayes, A.P., Vourlidas, A., Howard, R.A.: 2001, *Astrophys. J.* **548**, 1081.
Kohl, J.L., Esser, R., Gardner, L.D., Habbal, S., Daigneau, P.S., Dennis, E.F., Nystrom, G.U., Panasyuk, A., Raymond, J.C., Smith, P.L., Strachan, L., *et al.*: 1995, *Solar Phys.* **162**, 313.
Koutchmy, S., Lamy, P.: 1985, *Properties and Interactions of Interplanetary Dust*, *ASSL* **119**, *IAU Colloq.* **85**, 63.
Llebaria, A., Lamy, P.L., Danjard, J.-F.: 2006, *Icarus* **182**, 281.
Llebaria, A., Loirat, J., Lamy, P.: 2010, *SPIE* **7533**, 75330.
Louis, A.K., Natterer, F.: 1983, *Proc. IEEE* **71**, 379.
Manchester, W. IV, Gombosi, T., DeZeeuw, D., Sokolov, I., Roussev, I., Powell, K., Kota, J., Toth, G., Zurbuchen, T.: 2005, *Astrophys. J.* **622**, 1225.
Minnaert, M.: 1930, *Z. Astrophys.* **1**, 209.
Moran, T.G., Davila, J.M.: 2004, *Science* **305**, 66.
Morgan, H., Habbal, S.R.: 2007, *Astron. Astrophys. Lett.* **471**, L47.
Morgan, H., Habbal, S.R.: 2010, *Astrophys. J.* **710**, 1.
Morgan, H., Habbal, S.R., Lugaz, N.: 2009, *Astrophys. J.* **690**, 1119.
Quémerais, E., Lamy, P.: 2002, *Astron. Astrophys.* **393**, 295.
Schuster, A.: 1897, *Mon. Not. R. Astron. Soc.* **40**, 35.
van de Hulst, H.C.: 1950, *Bull. Astron. Inst. Netherlands* **11**(410), 150.
Vásquez, A.M., Frazin, R.A., Hayashi, K., Sokolov, I.V., Cohen, O., Manchester, W.B. IV: 2008, *Astrophys. J.* **682**, 1328.